IEEE Journal of Microwaves

Received 22 December 2020; accepted 27 January 2021. Date of publication 23 March 2021; date of current version 7 April 2021.

Digital Object Identifier 10.1109/JMW.2021.3055869

A Computationally Efficient Reconstruction Approach for Imaging Layered Dielectrics With Sparse MIMO Arrays

INGRID ULLMANN AND MARTIN VOSSIEK

(Invited Paper)

Friedrich-Alexander University Erlangen-Nuremberg, Erlangen 91058, Germany

CORRESPONDING AUTHOR: Ingrid Ullmann (e-mail: ingrid.ullmann@fau.de).

ABSTRACT This contribution presents a novel, computationally efficient approach to radar imaging of layered dielectrics with sparse MIMO arrays. Our concept does not impose any constraints on the array topology and at the same time promises to be more efficient than the state-of-the-art backprojection algorithm because it can make use of *k*-space reconstruction schemes. Experimental results with a sparse, non-equidistantly sampled array are provided. These demonstrate the feasibility of the approach and that the computational burden could be reduced by several orders of magnitude in a given practical example related to radar based non-destructive testing.

INDEX TERMS Array signal processing, millimeter-wave imaging, MIMO, nondestructive testing, radar imaging.

I. INTRODUCTION

Multiple-input-multiple-output (MIMO) radars are state of the art in radar imaging for security screening and other applications. In contrast to the synthetic aperture radar (SAR) technique where an antenna is moved to span a synthetic aperture, MIMO exploits spatial diversity using many antennas, which makes it real-time capable. MIMO arrays are often designed as sparse periodic arrays so that their effective aperture equals a full array [1], [2]. This offers the same image resolution as full arrays but requires much less antennas and hardware.

For image reconstruction, the measurement data can be processed in the space domain or the spatial frequency domain (also termed wavenumber domain or *k*-space). The backprojection algorithm (BPA), as described in e.g., [3], is a space domain solution to the linearized inverse scattering problem. It can be applied to any kind of array topology and yields highly focused images but it is very time-consuming because the signals of all transmitter (TX) and receiver (RX) combinations have to be processed separately. For monostatic imaging systems, the reconstruction can more efficiently take place in the wavenumber domain [4]. Typical reconstruction algorithms include the Phase Shift Migration (PSM) [5] and the Range Migration Algorithm (RMA) [6], which originate from geophysical remote sensing but are easily adoptable to monostatic radar imaging [7], [8]. However, for MIMO systems, a wavenumber domain reconstruction is not that easy. This is because the PSM and RMA use a two-way propagation term which accounts for the identical location of TX and RX, but obviously cannot be applied to multistatic or MIMO systems. A number of reconstruction concepts have been proposed to address this issue, seeking to make MIMO image reconstruction faster by introducing wavenumber-domain techniques as well. However, most of them represent either approximations or impose constraints on the topology of the MIMO array. Among such techniques are multistatic-to-monostatic-conversion schemes [9], [10] that calculate a hypothetical monostatic aperture and compensate the resulting phase error by a reference term. Publication [11] suggested a subsampling scheme in *k*-space followed by a fusion into one image. An adjustment of the PSM and RMA to MIMO arrays was presented in [12] and [13], respectively. Here, a reorganization of the 4D-MIMO data in $k_{x,\mathrm{TX}}$, $k_{y,\mathrm{TX}}$, $k_{x,\mathrm{RX}}$, $k_{y,\mathrm{RX}}$ to a common 2D data set in k_x and k_y is proposed. The resulting accumulated data are processed with the usual steps of the PSM or RMA. However, for fusing the data, the TX and RX arrays must have the same length and step size [14]. Other approaches include the ones proposed in [14] or [15], which impose constraints on the topology of

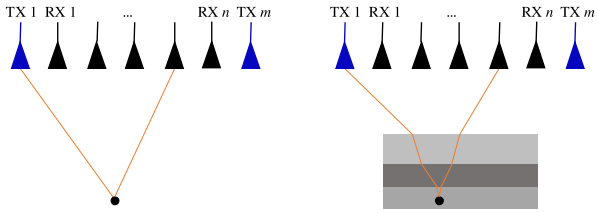

FIGURE 1. Illustration of different MIMO imaging scenarios: Single-medium background (left) and multilayer scenario where the refracted wave propagation needs to be taken into account for an undisturbed image reconstruction (right).

the MIMO array, e.g., that arrays have to fulfil the Nyquist sampling criterion [15] or that the receive data have to be equidistantly sampled [14]. For non-equidistantly sampled data, a reconstruction algorithm based on a non-uniform fast Fourier transform (NUFFT) was presented in [16]. However, NUFFTs are generally cumbersome in calculation.

We build our approach on the ones presented in [14] and [17]. Here, a reconstruction concept for MIMO systems is presented that operates in the Fourier domain for as much as possible. The general idea is to partition the multi-transmitter system into a sum of single-transmitter systems. The receive data of each single transmitter are processed together in the wavenumber domain using fast k-space techniques. This makes the computation more efficient than the BPA because only the transmitters have to be processed separately, whereas the receivers can be treated as an array in the Fourier domain. Parallelization is possible, which promises to make this kind of reconstruction fast [17].

In contrast to [14], which requires the RX array to be equidistantly sampled, the reconstruction algorithm in [17] can be used to any kind of array topology, e.g., it is also applicable with sparse arrays that are not equidistantly sampled. Therefore, this approach, which will be elaborated in Sec. II, is the basis for our reconstruction concept. However, the concept in [17] only deals with free-space propagation of the electromagnetic waves. Such a scenario is well suited for e.g., security screening of persons where the clothing is hardly interfering with millimetre-waves. But it is not suited for imaging structures of layered dielectrics, which is a typical scenario in non-destructive testing (such as, e.g., radome testing) or ground penetrating radar. The focus of this paper is directed towards this application area and for the first time a solution to overcome the previously mentioned limitations is presented

When introducing a multi-material background, the image reconstruction becomes considerably more complex compared to the classical image reconstruction that assumes free-space propagation of the electromagnetic waves. In a multi-material background, changing phase velocities and resulting wave refraction, as illustrated in Fig. 1, need to be taken into account.

The backprojection algorithm can readily be extended to multilayered media. When doing so, a ray tracing step has to be introduced [18] in order to include the refracted optical paths from TX to target and back to RX, which makes the algorithm still more costly with respect to computation.

For monostatic systems, also the PSM algorithm is easily adjusted to a multilayer scenario with planar material boundaries [19]. Its computation is much faster than adjusting the BPA to multilayered media. However, while PSM has been adopted to MIMO systems in e.g., [12] and [14], still there has not been a concept for arbitrary MIMO arrays because the proposed techniques will only work with certain array topologies as mentioned above.

Therefore, the contribution of this paper is a reconstruction algorithm that yields high-resolution images of layered dielectrics, making use of the efficient Fourier imaging and being applicable to any kind of MIMO array.

The rest of the paper is organized as follows: In Sec. II the proposed reconstruction algorithm is derived based on the strategy from [17]. Sec. III presents experimental results. In Sec. IV, the concept is compared to the state of the art w.r.t. computational cost. Finally, Sec. V draws a conclusion.

II. IMAGE RECONSTRUCTION CONCEPT

A. FFT-BASED IMAGE RECONSTRUCTION FOR SPARSE MIMO ARRAYS

Consider the linearized electromagnetic scattering problem for a MIMO system when the aperture is rectangular along the x and y directions, at $z = 0$:

$$E_{\text{scat}}(x_{\text{TX}}, y_{\text{TX}}, x_{\text{RX}}, y_{\text{RX}}, z = 0, \omega) = \iiint o(x, y, z_0) \exp\left\{-jk\sqrt{(x-x_{\text{TX}})^2+(y-y_{\text{TX}})^2+z_0^2}\right\} \exp\left\{-jk\sqrt{(x_{\text{RX}}-x)^2+(y_{\text{RX}}-y)^2+z_0^2}\right\} dx dy dz \quad (1)$$

In (1), $E_{scat}(x_{\text{TX}}, y_{\text{TX}}, x_{\text{RX}}, y_{\text{RX}}, z = 0, \omega)$ is the scattered field at specific transmitter and receiver locations, denoted by indices "TX" and "RX", and frequency ω. Furthermore, $o(x, y, z_0)$ denotes the object distribution, and the exponential terms equal the Green's functions (neglecting amplitudes), which describe wave propagation from transmitter to target and from target to receiver, respectively.

Obtaining an image $o'(x, y, z_0)$ of the object distribution means solving the inverse scattering problem,

$$o'(x, y, z_0) = \int\int\int\int\int E_{scat}(x_{\text{TX}}, y_{\text{TX}}, x_{\text{RX}}, y_{\text{RX}}, 0, \omega) \exp\left\{+jk\sqrt{(x-x_{\text{TX}})^2+(y-y_{\text{TX}})^2+z_0^2}\right\} \exp\left\{+jk\sqrt{(x_{\text{RX}}-x)^2+(y_{\text{RX}}-y)^2+z_0^2}\right\} dx_{\text{TX}} dx_{\text{RX}} dy_{\text{TX}} dy_{\text{RX}} d\omega. \quad (2)$$

The exponential terms in (2) equal the complex conjugate of the Green's functions in TX and RX.

Solving the MIMO imaging problem (2), is possible by the backprojection algorithm in the space domain when directly implementing (2) with sums. Obviously, this is computationally demanding. The more efficient, k-space-based concept

will be described in the following. For a detailed derivation we refer to [14] or [17].

For each i-th transmitter, the corresponding receive data are treated separately. The first step then is to Fourier transform the RX data to k-space along the lateral dimensions x_{RX} and y_{RX}:

$$E_{\mathrm{scat}}\left(x_{\mathrm{TX,i}}, y_{\mathrm{TX},i}, k_x, k_y, 0, \omega\right) = \mathrm{FT}\left\{E_{\mathrm{scat}}\left(x_{\mathrm{TX},i}, y_{\mathrm{TX},i}, x_{\mathrm{RX}}, y_{\mathrm{RX}}, 0, \omega\right)\right\} \quad (3)$$

In (3), FT denotes Fourier transforms w.r.t. x and y, which will be implemented as fast Fourier transforms (FFT).

The k-space data are then backpropagated from the aperture plane $z = 0$ to the range of the target, z_0, by multiplication with a propagator term which is equal to the complex conjugate of the RX Green's function in k-space

$$E(x_{TX,i}, y_{TX,i}, k_x, k_y, z_0, \omega) = E_{\mathrm{scat}}\left(x_{TX,i}, y_{TX,i}, k_x, k_y, 0, \omega\right) \cdot G_{\mathrm{RX}}\left(k_x, k_y, z_0, \omega\right)^{*}. \quad (4)$$

The k-space Green's function $G_{\mathrm{RX}}(k_x, k_y, z_0, \omega)$ can be obtained either by Fourier transforming the RX Green's function's space domain formulation (the lowermost term in (1)) or directly in the wavenumber domain. Again neglecting amplitude terms, the wavenumber domain Green's function for the RX path is

$$G_{\mathrm{RX}}\left(k_x, k_y, z_0, \omega\right) = \exp\left\{-j\, k_z\, z_0\right\}, \quad (5)$$

where k_z can be deduced from the dispersion relation for one-way propagation:

$$k_z = \sqrt{k^2 - k_x^2 - k_y^2}. \quad (6)$$

Here, k is the wavenumber and k_x and k_y are the wavenumber components in x and y directions corresponding to the RX array.

It is important to mention that a Fourier transform of non-equidistantly sampled receive data can be performed nevertheless when filling the non-sampled positions with zeros in order to create a pseudo-equidistant sampling [17]. This approach is termed "special zero-padding" in [17] and will be termed "spatial zero padding" in this paper to underline its meaning. Of course, with this approach we will only obtain a good image if the sparse array is reasonably designed, i.e., so that its effective aperture is full or at least provides a point spread function with low sidelobe level.

In addition to backpropagating the RX data, the propagation of the electromagnetic wave from the transmitter to the target,

$$g_{\mathrm{TX}}\left(x, y, x_{\mathrm{TX},i}, y_{\mathrm{TX},i}, z_0, \omega\right) = \exp\left\{-jk\sqrt{(x-x_{\mathrm{TX},i})^2 + (y-y_{\mathrm{TX},i})^2 + z_0^2}\right\} \quad (7)$$

(cf. (1)) has to be considered for the i-th transmitter. (7) is the space domain formulation of the TX Green's function since this term must be accounted for in the space domain, cf. [14] or [17]. Therefore, an inverse Fourier transform is first performed to the backpropagated receive data from (4) and then the complex conjugate of the term in (7) is multiplied to it.

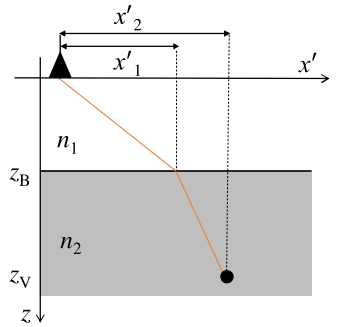

FIGURE 2. Geometry for determination of refracted wave propagation according to [22].

To focus an image, all frequency steps and all transmitters are then summed up.

In sum, the reconstruction reads as

$$o'(x, y, z_0) = \sum_{\mathrm{TX}} \sum_{\omega} g_{\mathrm{TX}}(x, y, x_{\mathrm{TX},i}, y_{\mathrm{TX},i}, z_0, \omega)^{*} \cdot \mathrm{IFT}\{E_{\mathrm{scat}}(x_{\mathrm{TX},i}, y_{\mathrm{TX},i}, k_x, k_y, 0, \omega) \cdot G_{\mathrm{RX}}(k_x, k_y, z_0, \omega)^{*}\} \quad (8)$$

where IFT denotes the two-dimensional inverse Fourier transform w.r.t. k_x and k_y.

B. EXTENSION TO MULTILAYERED MEDIA

Eq. (8) can be used for a single-medium imaging scenario. For a heterogeneous background, however, the Green's functions for the TX and RX paths have to be adjusted. The RX Green's function for multilayered media with planar material boundaries is

$$G_{\mathrm{RX}}\left(k_x, k_y, z_j, \omega\right) = \exp\left\{-j\, k_{z,j}\, (z_j - z_{j-1})\right\} \quad (9)$$

i.e., the wavenumber is adjusted to the wavenumber of the j-th medium:

$$k_{z,j} = \sqrt{k_j^2 - k_x^2 - k_y^2}. \quad (10)$$

and the field data are propagated to the respective material boundaries z_j for each layer. Note that (9) is valid only for planar material boundaries.

The TX Green's function, (7), however, is a space domain formulation. In that case, the refracted path from the i-th transmitter to the target with the material boundaries in between has to be considered, see Fig. 1.

To the seemingly simple problem of finding the refracted path from antenna to target, in general, there is no analytic solution. The wave propagation path (also termed optical path) has to be found numerically, using ray tracing methods [20], [21].

Only for a planar material boundary separating two half-spaces, an analytic formulation for the optical path can be found [22]. For that we regard the corresponding geometry in Fig. 2. Since the incident and refracted waves are coplanar [23], the 3D problem can be recast into a 2D problem in that plane. Its lateral coordinate is denoted x' in Fig. 2, where x'_1 denotes the distance between the TX antenna's lateral coordinate and the unknown refraction point. Further, x'_2

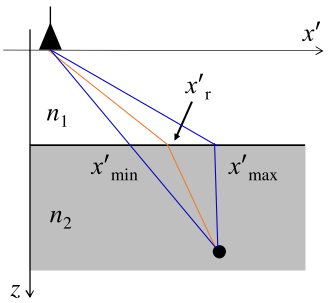

FIGURE 3. Geometry for determination of refracted wave propagation according to [24].

is the (known) distance between the antenna and the image voxel. The depths of the material boundary and the voxel which we want to focus are z_B and z_V, respectively. The terms n_1 and n_2 denote the refractive indices of the media, which for dielectric materials equal the square roots of the relative permittivities.

The refracted optical path has to satisfy Snell's law of refraction (assuming object dimensions much larger than the wavelength so that geometrical optics can be used),

$$n_1 \cdot \sin\alpha = n_2 \cdot \sin\beta. \tag{11}$$

Expressing (11) in the variables x'_1 and x'_2 yields

$$n_1 \frac{x'_1}{\sqrt{z_B^2 + (x'_1)^2}} = n_2 \frac{x'_2 - x'_1}{\sqrt{(z_V - z_B)^2 + (x'_2 - x'_1)^2}}, \tag{12}$$

a fourth-order equation in x'_1 [22]. Solving this equation for x'_1 will determine the optical path. However, a fourth-order equation will obviously yield four solutions. Thus, such an approach can be used since only one solution is sensible, but it requires the extra step of finding the correct solution out of four possible ones.

Another solution to finding the optical path for a system consisting of two half-spaces can be found in [24]: Here, an empirical approximation is proposed, onto which we build in this paper. The corresponding geometry is shown in Fig. 3. As in Fig. 2, the 2D geometry representing the plane of the incident and refracted waves is depicted.

Again, we want to retrieve the refracted wave path between transmit antenna, material boundary and voxel (orange in Fig. 1). The path is determined by the refraction point x'_r. For the refraction point x'_r, [24] proposed the empirical approximation

$$x'_r = x'_{\max} + \frac{n_1}{n_2}(x'_{\min} - x'_{\max}) \tag{13}$$

where $x'_{\min}$ and $x'_{\max}$ represent the coordinates shown in Fig. 3, which correspond to the two extreme paths possible: when there is no refraction ($x'_{\min}$) and when there is maximum refraction ($x'_{\max}$). The terms n_1 and n_2 again denote the refractive indices of the media.

With the approximation in (13), the refraction point and thus the refracted optical path can be found. The results are the basis to form the TX propagation term as

$$\begin{aligned} &g_{\mathrm{TX}}\left(x, y, x_{\mathrm{TX},i}, y_{\mathrm{TX},i}, z_0, \omega\right) \\ &= \exp\left\{-jk\left[n_1\sqrt{(x_{r,i} - x_{\mathrm{TX},i})^2 + (y_{r,i} - y_{\mathrm{TX},i})^2 + z_1^2}\right.\right. \\ &\quad \left.\left. + n_2\sqrt{(x - x_{r,i})^2 + (y - y_{r,i})^2 + (z_2 - z_1)^2}\right]\right\} \end{aligned} \tag{14}$$

For a two-layer medium the overall reconstruction formula then is

$$\begin{aligned} &o'(x, y, z_0) \\ &= \sum_{\mathrm{TX}}\sum_{\omega} \exp\left\{+jk\left[n_1\sqrt{(x_{r,i} - x_{\mathrm{TX},i})^2 + (y_{r,i} - y_{\mathrm{TX},i})^2 + z_1^2}\right.\right. \\ &\quad \left.\left. + n_2\sqrt{(x - x_{r,i})^2 + (y - y_{r,i})^2 + (z_2 - z_1)^2}\right]\right\} \\ &\quad \cdot \mathrm{IFT}\left\{E_{\mathrm{scat}}\left(x_{\mathrm{TX,i}}, y_{\mathrm{TX,i}}, k_x, k_y, 0, \omega\right)\right. \\ &\quad \left. \cdot \exp\left\{+jk_{z,1}z_1\right\} \cdot \exp\left\{+jk_{z,2}(z_2 - z_1)\right\}\right\}. \end{aligned} \tag{15}$$

A flow diagram of the proposed algorithm is shown in Fig. 4 to illustrate the procedure.

The approximation in (14) as well as the solution to the fourth-order equation in (12) are applicable to two-layer media (i.e., air and one dielectric). Other approximations for such a scenario were proposed in [25] and [26]. For multilayered media, a ray tracing step is needed. Among commonly employed techniques are ray shooting and ray bending [27] or Eikonal solvers [28] based on the Fast Marching Method [29].

III. EXPERIMENTAL VERIFICATION

A. TEST SETUP

To demonstrate our concept, we imaged a Siemens star behind a PVC (polyvinylchloride) plate. A Siemens star is an object often used to evaluate the resolution of imaging systems. The test object employed in our measurements is shown in Fig. 5.

Thus, when scanning the test object, we obtain a two-media background consisting of air and PVC with the Siemens star as target to be imaged.

As a scanning system we used a *Rohde & Schwarz QAR* scanner (see [30]). *QAR* is a MIMO radar consisting of 3 × 4 sparse subarrays with spacing in between (see [30]). Because of the small size of the test object, only 3 × 3 blocks of the *QAR* are evaluated. The array topology of the resulting MIMO system is shown in Fig. 6. It consists of 9 blocks of 2 times 47 transmitters and 2 times 47 receivers each, which are orientated as in Fig. 6. Thus, 846 TX and 846 RX channels contribute to the measurements. The spacing between the antennas within one block is 3 mm.

The applied transmit signal is a 64-point stepped-frequency-continuous-wave (SFCW) signal, from 74 GHz to 79 GHz.

For the measurement, the PVC plate was placed parallel to the array, at a distance of 60.5 cm. With the plate thickness of 3 cm, the star is located 63.5 cm from the aperture plane.

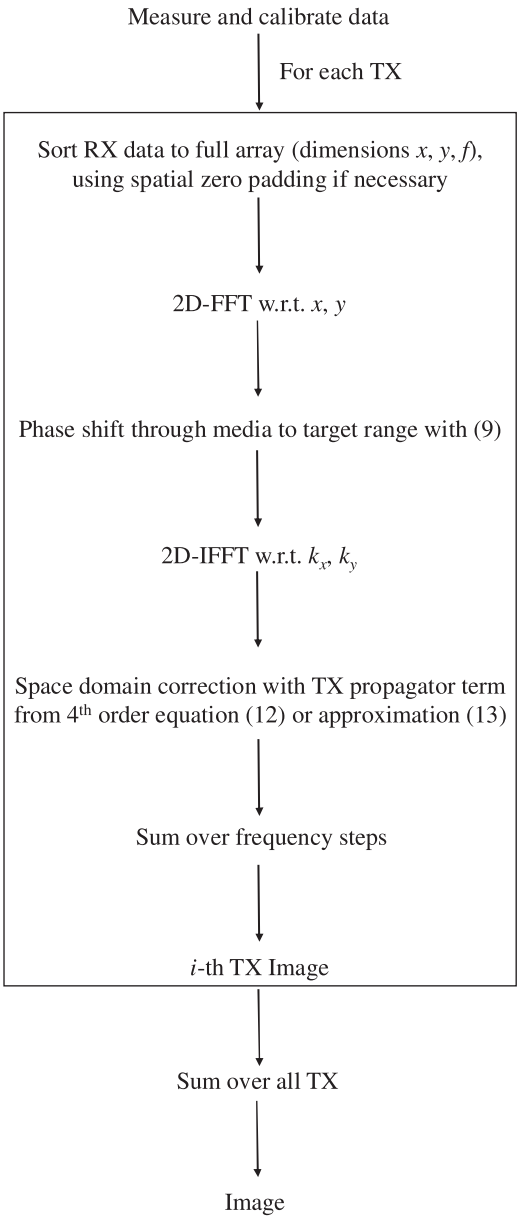

FIGURE 4. Flow diagram of the proposed MIMO image reconstruction algorithm.

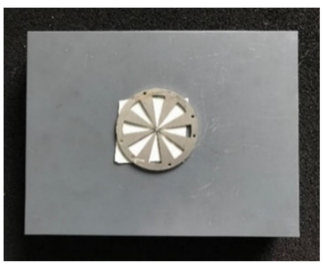

FIGURE 5. Test object: Siemens star on PVC plate. Plate dimensions: 20 cm x 15 cm, depth 3 cm. Star dimensions: diameter 6 cm, thickness 1.5 mm. The object is scanned so that the Siemens star is on the plate's backside, not facing the antenna array (i.e., photograph displays rear view of scanning scene). The Siemens star was stuck to the PVC plate with adhesive tape (white rectangular area in the picture). Due to the small thickness of the adhesive tape, it has no noticeable effect on the imaging result.

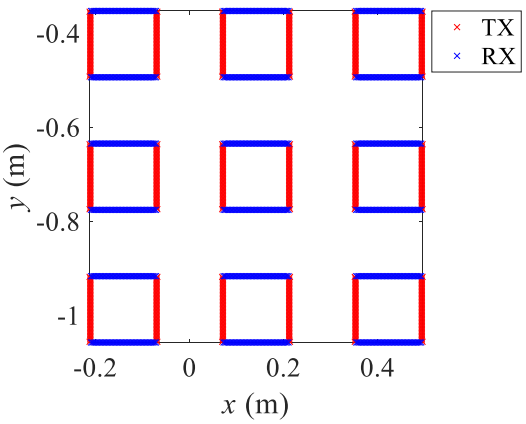

FIGURE 6. Employed MIMO array topology.

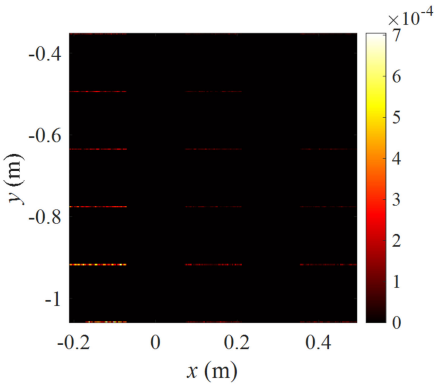

FIGURE 7. Amplitude of receive data at TX no. 423 and frequency step no. 1 after spatial zero padding. The amplitude values are w.r.t. the *QAR*'s internal normalization calibration.

The complex baseband signal measurement data from the *QAR* were then transferred to a PC for further processing and the evaluation of our proposed algorithm.

B. RECONSTRUCTION

According to Sec. II, the data are partitioned to form sub-datasets for all transmitters. For each transmitter individually, the sparse receive array data are filled with zeros at the spaces in between antenna positions. This is illustrated in Fig. 7, where the dataset for an exemplary TX position for one frequency step is shown. In the figure, the dataset that will be processed for the particular TX and frequency step is shown. As can be seen, there are non-zero entries at all receiver positions (cf. Fig. 6). All other entries are zero because there is no RX antenna at the corresponding positions. Nonetheless, an image reconstruction is fully possible as will be shown in the following section.

The reconstruction was then performed according to Sec. II-B with wave propagation through air and PVC (refractive index $n_{\mathrm{PVC}} \approx 1.6$). The wavenumbers k_x and k_y are retrieved from the spacing in the pseudo-equidistantly sampled aperture. In our measurement the spacing between antennas (and zeros) is 3 mm in both directions and accordingly, the wavenumber axes range from $-\pi/3$mm to $+\pi/3$mm. The

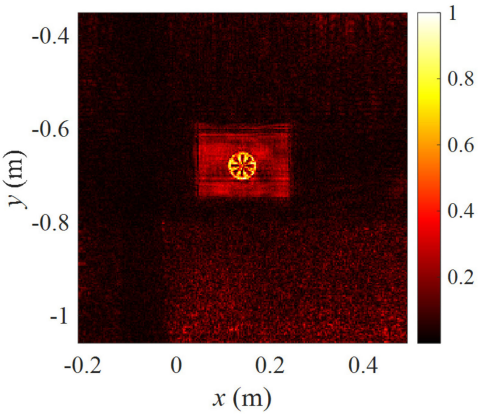

FIGURE 8. Image reconstruction (normalized) with the proposed concept.

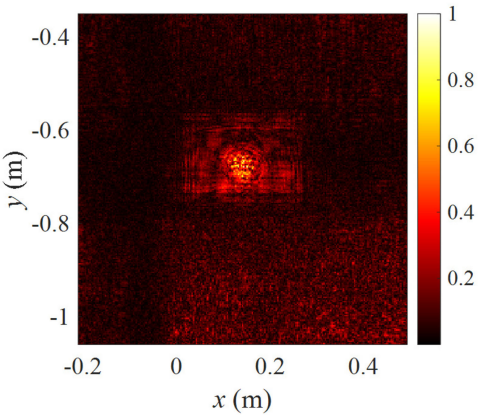

FIGURE 9. Image reconstruction (normalized) assuming free-space propagation.

approximation in (13) and (14) was used to calculate the TX Green's function.

C. RESULTS

Fig. 8 shows the image reconstructed with the proposed concept in the range of the Siemens star. As can be seen, the Siemens star behind the PVC plate is depicted clearly, which verifies the proposed reconstruction algorithm. For comparison, an image reconstruction according to the scheme in [17] (assuming free-space propagation of the electromagnetic waves) is shown in Fig. 9. The Siemens star now appears blurred and is not recognizable, which underlines the importance of including the material properties into imaging of layered media as proposed.

IV. COMPUTATIONAL EFFICIENCY

Obviously, using a free-space-based reconstruction is not satisfying. To obtain an image of equally high quality as with our algorithm, the BPA could be used. Its computational cost, however, is much higher. To quantify this, the computational complexities of the single steps in Fig. 4 are compared to the BPA (cf. (2)). The results can be found in Tables 1 and 2, respectively. Here, we assume a scenario as in the example in Sec. III, i.e., two layers and one target range to be imaged.

TABLE 1. Computational Complexity of Proposed Algorithm

Step	Complexity
2D FFT	$N_x \cdot N_y \cdot N_f \cdot \log_2(N_x \cdot N_y \cdot N_f)$
Phase Shifts	$2 \cdot N_x \cdot N_y \cdot N_f$
2D IFFT	$N_x \cdot N_y \cdot N_f \cdot \log_2(N_x \cdot N_y \cdot N_f)$
TX term	$N_{\mathrm{Tx},x} \cdot N_{\mathrm{Tx},y} \cdot N_x \cdot N_y$
Sum over frequencies	$N_x \cdot N_y \cdot N_f$
Sum over TX	$N_{\mathrm{Tx},x} \cdot N_{\mathrm{Tx},y} \cdot N_x \cdot N_y$
Total number of calculation steps (for $N_{\mathrm{Tx}} = N_{\mathrm{Rx}} = 84$; $N_x = N_y = 235$; $N_f = 64$)	**approx. $3.5 \cdot 10^8$**

TABLE 2. Computational Complexity of Standard BPA

Step	Complexity
Compute optical paths	$N_{\mathrm{Tx},x} \cdot N_{\mathrm{Tx},y} \cdot N_x \cdot N_y + N_{\mathrm{Rx},x} \cdot N_{\mathrm{Rx},y} \cdot N_x \cdot N_y$
Reconstruction	$N_{\mathrm{Tx},x} \cdot N_{\mathrm{Tx},y} \cdot N_{\mathrm{Rx},x} \cdot N_{\mathrm{Rx},y} \cdot N_x \cdot N_y \cdot N_f$
Total number of calculation steps (for $N_{\mathrm{Tx}} = N_{\mathrm{Rx}} = 84$; $N_x = N_y = 235$; $N_f = 64$)	**approx. $1 \cdot 10^{13}$**

In the considerations, the sorting step of the RX data is omitted because it can be implemented directly in the measurement when storing the captured data in a pre-allocated numerical array whose dimensions equal the pseudo-full antenna array dimensions.

The use of one FFT and one IFFT has a computational complexity of $N_x \cdot N_y \cdot N_f \log_2(N_x \cdot N_y \cdot N_f)$ each, where N_x and N_y are the number of sampling points in the x and y directions and N_f is the number of frequency steps. Additionally, the phase shift has a complexity of $N_x \cdot N_y \cdot N_f$ each for the two layers. The computation of the TX Green's function with (13) needs to be performed for all TX and all voxels in the image plane.

In contrast, when using the BPA, all receivers are treated separately, like the transmitters. Therefore, the RX Green's functions will have to be calculated from (13) too. This step is termed "Compute optical paths" in Table 2.

As could be seen, the TX part is equal in both algorithms. The advantage of our concept lies in the treatment of the receivers as an array in the Fourier domain. The brute-force reconstruction in the BPA needs to be performed for all antennas, voxels and frequencies resulting in a much higher computational load. As an example, in the measurement presented in Sec. III, the numbers of transmitters and receivers are $N_{\mathrm{Tx}} = N_{\mathrm{Rx}} = 846$, the numbers of sample points in x and y are $N_x = N_y = 235$ and the number of frequency steps is $N_f = 64$. With these numbers, the total cost of computation for the BPA is in the range of around 10^{13} operations, whereas our proposed concept only requires approximately $3.5 \cdot 10^8$ operations. These results impressively show the dramatic reduction in computational effort by several orders of magnitude that is achieved by the proposed reconstruction concept without impairing the imaging quality. The image quality is not impaired in any way compared to the previously known brute force methods.

V. CONCLUSION

We presented a novel, highly efficient approach to subsurface imaging of multilayered dielectrics with large sparse MIMO arrays. The proposed MIMO imaging scheme evaluates the complete RX data in the *k*-space for each TX separately, thus augmenting computational efficiency compared to the backprojection algorithm. Arbitrary sparse arrays can be treated when applying a spatial zero-padding step to the sparse array data. To account for changes in the background material, commonly used techniques from subsurface imaging were introduced into the reconstruction algorithm. With the proposed concept, high-resolution imaging was successfully demonstrated.

REFERENCES

[1] F. Gumbmann and L.-P. Schmidt, "Millimeter-wave imaging with optimized sparse periodic array for short-range applications," *IEEE Trans. Geosci. Remote Sens.*, vol. 49, no. 10, pp. 3629–3638, Oct. 2011.

[2] S. S. Ahmed, A. Schiessl, and L.-P. Schmidt, "A novel fully electronic active real-time imager based on a planar multistatic sparse array," *IEEE Trans. Microw. Theory Techn.*, vol. 59, no. 12, pp. 3567–3576, Dec. 2011.

[3] S. S. Ahmed, A. Schiessl, F. Gumbmann, M. Tiebout, S. Methfessel, and L.-P. Schmidt, "Advanced microwave imaging," *IEEE Microw. Mag.*, vol. 13, no. 6, pp. 26–43, Sep./Oct. 2012.

[4] D. M. Sheen, D. L. McMakin, and T. E. Hall, "Three-dimensional millimeter-wave imaging for concealed weapon detection," *IEEE Trans. Microw. Theory Techn.*, vol. 49, no. 9, pp. 1581–1592, Sep. 2001.

[5] J. Gazdag, "Wave equation migration with the phase-shift method," *Geophysics*, vol. 43, no. 7, pp. 1342–1351, Dec. 1978.

[6] R. H. Stolt, "Migration by Fourier transform," *Geophysics*, vol. 43, no. 1, pp. 23–48, Feb. 1978.

[7] C. Cafforio, C. Prati, and F. Rocca, "SAR data focusing using seismic migration techniques," *IEEE Trans. Aerosp. Electron. Syst.*, vol. 27, no. 2, pp. 194–207, Mar. 1991.

[8] I. G. Cumming and F. H. Wong, *Digital Processing of Synthetic Aperture Radar Data*. Norwood, MA, USA: Artech House, 2005.

[9] M. Soumekh, "Bistatic synthetic aperture radar inversion with application in dynamic object imaging," *IEEE Trans. Signal Process.*, vol. 39, no. 9, pp. 2044–2055, Sep. 1991.

[10] W. F. Moulder *et al.*, "Development of a high-throughput microwave imaging system for concealed weapons detection," in *Proc. IEEE Int. Symp. Phased Array Syst. Techn.*, Waltham, MA, USA, 2016, pp. 1–6.

[11] Y. Álvarez *et al.*, "Fourier-based imaging for multistatic radar systems," *IEEE Trans. Microw. Theory Techn.*, vol. 62, no. 8, pp. 1798–1810, Aug. 2014.

[12] H. Gao *et al.*, "Study of the extended phase shift migration for three-dimensional MIMO-SAR imaging in terahertz band," *IEEE Access*, vol. 8, pp. 24773–24783, Jan. 2020.

[13] R. Zhu, J. Zhou, G. Jiang, and Q. Fu, "Range migration algorithm for near-field MIMO-SAR imaging," *IEEE Geosci. Remote Sens. Lett.*, vol. 14, no. 12, pp. 2280–2284, Dec. 2017.

[14] G. Yang, C. Li, H. Gao, and G. Fang, "Phase shift migration with SIMO superposition for MIMO-sidelooking imaging at terahertz band," *IEEE Access*, vol. 8, pp. 208418–208426, Aug. 2020.

[15] X. Zhuge and A. G. Yarovoy, "A sparse aperture MIMO-SAR-based UWB imaging system for concealed weapon detection," *IEEE Trans. Geosci. Remote Sens.*, vol. 49, no. 1, pp. 509–518, Jan. 2011.

[16] B. Fan, J. Gao, H. Li, Z. Jiang, and Y. He, "Near-field 3D SAR imaging using a scanning linear MIMO array with arbitrary topologies," *IEEE Access*, vol. 8, pp. 6782–6791, Dec. 2019.

[17] M. Abbasi, A. Shayei, M. Shabany, and Z. Kavehvash, "Fast Fourier-based implementation of synthetic aperture radar algorithm for multistatic imaging system," *IEEE Trans. Instrum. Meas.*, vol. 68, no. 9, pp. 3339–3349, Sep. 2019.

[18] S. Tebaldini, T. Nagler, H. Rott, and A. Heilig, "Imaging the internal structure of an alpine glacier via L-band airborne SAR tomography," *IEEE Trans. Geosci. Remote Sens.*, vol. 54, no. 12, pp. 7197–7209, Dec. 2016.

[19] K. Gu, G. Wang, and J. Li, "Migration based SAR imaging for ground penetrating radar systems," *IEE Proc., Radar Sonar Navigat.*, vol. 151, no. 5, pp. 317–325, Oct. 2004.

[20] V. Cerveny, *Seismic Ray Theory*. Cambridge, MA, USA: Cambridge Univ. Press, 2001.

[21] Y. Huang, J. Zhang, and Q. H. Liu, "Three-dimensional GPR ray tracing based on wavefront expansion with irregular cells," *IEEE Trans. Geosci. Remote Sens.*, vol. 49, no. 2, pp. 679–687, Feb. 2011.

[22] A. Heinzel *et al.*, "Focusing methods for ground penetrating MIMO SAR imaging within half-spaces of different permittivity," in *Proc. Eur. Conf. Synthetic Aperture Radar*, Hamburg, Germany, 2016, pp. 1–5.

[23] M. Born and E. Wolf, *Principles of Optics*, vol. 4. London, U.K.: Pergamon Press, 1970.

[24] E. M. Johansson and J. E. Mast, "Three-dimensional ground-penetrating radar imaging using synthetic aperture time-domain focusing," *Proc. SPIE 2275, Adv. Microw. Millimeter-Wave Detectors*, vol. 2275, pp. 205–214, Sep. 1994.

[25] C. Rappaport, "A novel, non-iterative, analytic method to find the surface refraction point for air-coupled ground penetrating radar," in *Proc. Eur. Conf. Antennas Propag.*, 2011, pp. 1786–1789.

[26] N. Milisavljevic and A. G. Yarovoy, "An effective algorithm for subsurface SAR imaging," in *Proc. IEEE Antennas Propag. Soc. Int. Symp.*, San Antonio, TX, USA, 2002, pp. 314–317.

[27] D. A. Waltham, "Two-point ray tracing using fermat's principle," *Geophys. J. Int.*, vol. 93, no. 3, pp. 575–582, Jun. 1988.

[28] J. Rickett and S. Fomel, "A second-order fast marching eikonal solver," Stanford Exploration Project Rep. 100, pp. 287–292, 1999.

[29] J. A. Sethian, "A fast marching level set method for monotonically advancing fronts," *Proc. Nat. Acad. Sci*, vol. 93, no. 4, pp. 1591–1595, 1996.

[30] [Online]. Available: https://www.rohde-schwarz.com/us/product/qar

INGRID ULLMANN is currently working toward the Ph.D. degree with the Institute of Microwaves and Photonics, Friedrich-Alexander University Erlangen-Nuremberg, Erlangen, Germany. Her research interests include radar imaging and radar signal processing for nondestructive testing, security, medical, and automotive applications. She is the group leader of the research group "Radar and Imaging Systems" at the Institute of Microwaves and Photonics and a reviewer for the European Radar Conference (EuRAD) and various journals in the field of microwaves.

She was the recipient of the Argus Science Award (sponsored by Airbus Defense and Space, now Hensoldt) for her master's thesis in 2016 and the Best Paper Award of the European Radar Conference in 2019.

MARTIN VOSSIEK (Fellow, IEEE) received the Ph.D. degree from Ruhr-Universität Bochum, Bochum, Germany, in 1996. In 1996, he joined Siemens Corporate Technology, Munich, Germany, where he was the Head of the Microwave Systems Group, from 2000 to 2003. Since 2003, he has been a Full Professor with the Clausthal University of Technology, Clausthal-Zellerfeld, Germany. Since 2011, he has been the Chair of the Institute of Microwaves and Photonics (LHFT), Friedrich-Alexander-Universität Erlangen-Nürnberg (FAU), Erlangen, Germany. He has authored or coauthored more than 300 articles. His research has led to more than 90 granted patents. His current research interests include radar, imaging techniques, RF identification, communication, and locating systems. He has been a member of organizing committees and technical program committees for many international conferences. He is a member of the German IEEE Microwave Theory and Techniques (MTT) or Antennas and Propagation (AP) Chapter Executive Board and the IEEE MTT-S Technical Coordinating Committees MTT-24, MTT-27, and MTT-29. He was the Founding Chair of the MTT IEEE Technical Coordinating Subcommittee MTT-27 Wireless-Enabled Automotive and Vehicular Application. He was the recipient of several international awards including the 2019 Microwave Application Award from the IEEE MTT Society (MTT-S). He was on the review boards for numerous technical journals. From 2013 to 2019, he was an Associate Editor for IEEE TRANSACTIONS ON MICROWAVE THEORY AND TECHNIQUES.